GRANT AGREEMENT No.: 764902 **Project Acronym: TOMOCON** **Project title: Smart tomographic sensors for advanced industrial process control**	TOMOCON Smart Tomographic Sensors for Advanced Industrial Process Control	
Deliverable Rel. No. **D3.3.**	Lead Beneficiary **INPT**	
EU Del. No. **D11**	Type **Report**	
WP No. **WP3**	Date: **06.09.2021**	Revision: **0**

Innovative Training Network

TOMOCON

Deliverable Title

Validation of Improved Multiphysics Modelling

Description

This report describes the improvements in multiphysics modelling and validation results gained from the use of tomographic imaging techniques and advanced numerical process simulations.

Prepared by:	Prof. Dr. Dominique Legendre	
Approved by:	Prof. Dr. Uwe Hampel	U. Ham
Approved by Supervisory Board:		07.09.2021

Dissemination Level: **Public**

This project has received funding from the European Union's Horizon 2020 research and innovation programme under the Marie Skłodowska-Curie Grant Agreement No. 764902.

Revision Sheet

Revision Number	Purpose of Revision	Effective Date
0	Initial Issue	07.09.2021

Dissemination Level: **Public**

This project has received funding from the European Union's Horizon 2020 research and innovation programme under the Marie Skłodowska-Curie Grant Agreement No. 764902.

Table of Contents

This project has received funding from the European Union's Horizon 2020 research and innovation programme under the Marie Skłodowska-Curie Grant Agreement No. 764902.

This project has received funding from the European Union's Horizon 2020 research and innovation programme under the Marie Skłodowska-Curie Grant Agreement No. 764902.

1. Inline fluid separation

1.1. Introduction

Inline fluid separation is a recent technology for gas extraction which makes use of a static swirl element installed inside the pipeline. This swirl element is characterized by deflected blades on its surface which transform part of the incoming axial momentum into a tangential one generating then centrifugal forces up to 100 times the gravitational acceleration. The centrifugal force pushes the heavy phase next to the wall while leaving the light one in the centre to be recovered at the outlet by a pick-up tube. The TOMOCON project aims at building a controller of the valve at the pick-up tube to insure a higher efficiency. The data used by the control unit is provided by two tomographic sensors namely a WMS and an ERT installed upstream and downstream the swirl element respectively. CFD simulations are also used to investigate and describe the swirling flow and the separation process to help defining the transfer function in the controller.

1.2. The numerical approach

To simulate such a complex process, a hybrid CFD approach is chosen and consists of using Immersed Boundary Method (IBM) [1] for solid/fluid interaction to simulate the pipe, the swirl element and the pick-up tube instead of using complex and demanding meshes. The flow being highly turbulent that DNS is not affordable, the turbulence is modelled via the Large Eddy Simulation (LES) [2] and more specifically the mixed dynamic Smagorinsky model. And to avoid mesh refinement next to the wall to capture the viscous sub-layer, an original wall model for hybrid LES/IBM is developed. When it comes to two-phase flows, two length scales are present in the separator: The bubble size and the separator size, the ratio of these two equals 1,000. Therefore, the Lagrangian Tracking [3] is used for the dispersed phase through the resolution of the trajectory equation of each bubble. If a bubble is in contact with an IB object, it rebounds according to the normal to the IB surface following a collision model which couples IBM/LES. After the swirl element, the bubbles start to migrate towards the pipe centre and once the accumulation takes place that the total volume of the dispersed phase in one cell is higher than the cell volume, a switch to Volume of Fluid (VoF) [4] is done to simulate the interface of the formed gas core.

1.3. The model validation

The CFD simulations within the scope of this project are carried out using an IMFT in-house code called JADIM. The solvers LES, IBM, LT and VoF were already validated separately through diverse studies [1, 2, 3, 4]. However, the new CFD developments proposed to build the hybrid approach are subject to validation tests. First, the use of IBM for complex geometry constructed using CAD software is validated via the simulation of the separator (see Fig. 1).

Dissemination Level: **Public**

This project has received funding from the European Union's Horizon 2020 research and innovation programme under the Marie Skłodowska-Curie Grant Agreement No. 764902.

Fig. 1: Visualization of the separator using IBM

Then, the wall model for IBM/LES is validated through the study of the classical turbulent pipe flow, the flow statistics are compared to previous experimental measurement and numerical simulations (see Fig. 2).

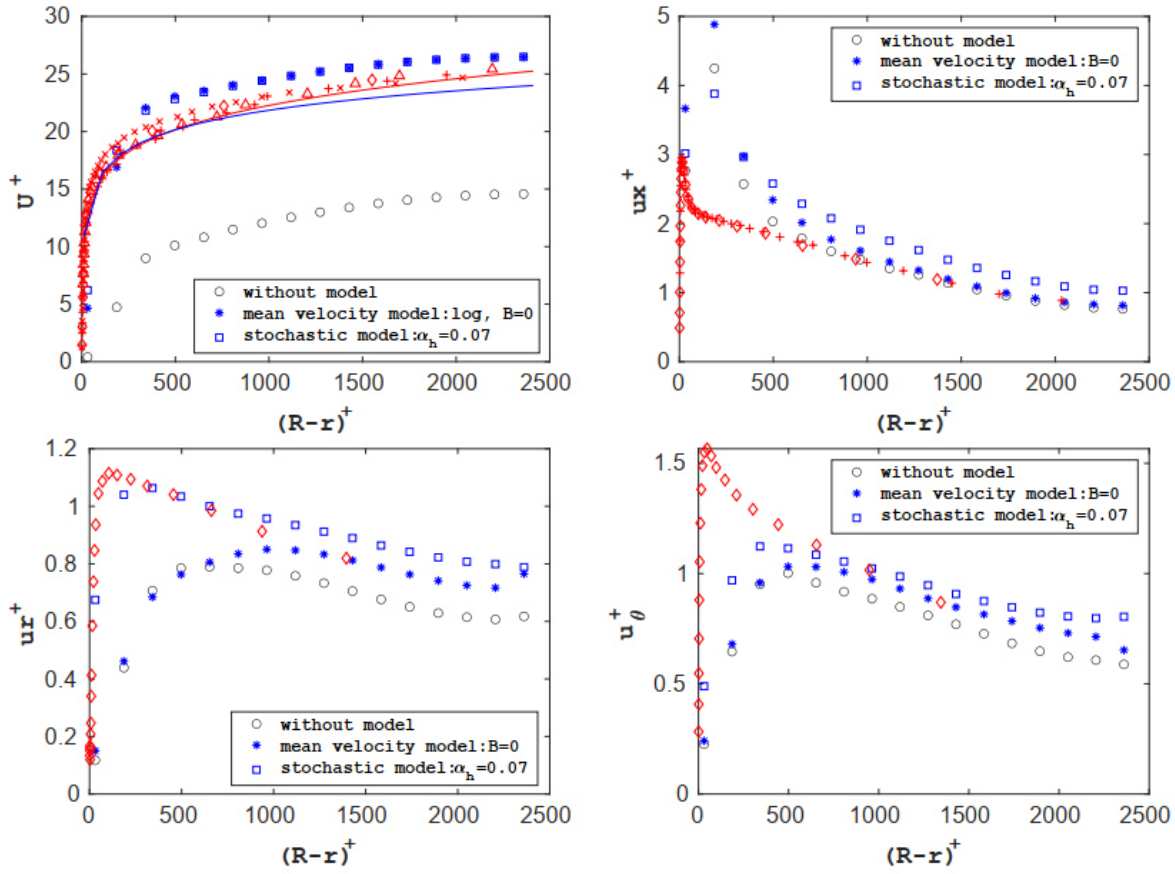

Fig. 2: Flow statistics of turbulent pipe flow for Re=100,000: Without a wall model (in black), with wall models (in blue) and reference results for validation (in red).

The validation of the collision model for IBM/LT is done through a test case of the two-phase flow simulation in the separator for Re=4,600 where a set of 1,000 bubbles of a radius of 1 mm are injected randomly upstream the swirl element with the fluid velocity. By comparing the numerical results of the simulation without (see Fig. 3a) and with the collision model (see Fig. 3b), the model seems to work as expected and the bubbles do not get trapped inside the IB objects.

This project has received funding from the European Union's Horizon 2020 research and innovation programme under the Marie Skłodowska-Curie Grant Agreement No. 764902.

Fig. 3a: Two-phase flow simulation without the collision model

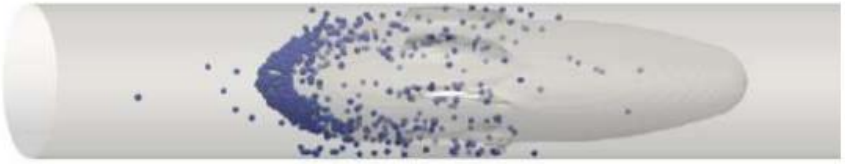

Fig. 3b: Two-phase flow simulation with the collision model

Finally, to test the hybrid LT/VoF, we consider 3D simulation of bubbles accumulation in a solid rotation fluid which is a close configuration to the swirling flow inside the separator. A set of 1,000 bubbles of a radius of 1 mm are injected randomly with the fluid velocity inside the pipe which has a constant angular velocity set to 0.3 rad/s. Fig. 4 shows the initialization state (at left) and the switching to VoF of the accumulated bubbles (right) where the core interface in blue is corresponding to a gas volume fraction equals 0.5.

Fig. 4: Two-phase flow simulation using hybrid LT/VoF

1.4. The numerical domain

To describe the pipe, the swirl element, the pick-up tube and the flow straightener which is located between the pipe and the pick-up tube to eliminate the swirling flow in that region, IBM is used in a domain of size Lx× Ly× Lz on a 3D Cartesian mesh made Nx× Ny× Nz where (Lx, Nx), (Ly, Ny) and (Lz, Nz) are the length and the number of cells along the x, y and z direction respectively. The x-direction corresponds to the axis of the pipe. The mesh is regular so that the grid size Δ is uniform along the three directions. The domain considered in the following is defined by Lx=0.92m, Ly= Lz =0.1m. The gravity is g=-9.81 ex.

1.5. The numerical results

1.5.1. Single-phase flow in the separator

Using LES/ IBM with the wall model, numerical simulation of swirling single-phase flow are performed for Re=50,000. Fig. 5 illustrates the flow streamlines along the separator. The maximal velocity is located at the blades.

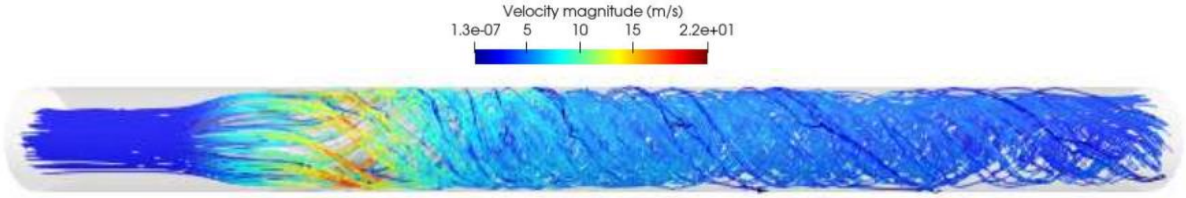

Fig. 5: Streamlines of swirling single-phase flow in the separator for Re=50,000

We can eventually extract the azimuthal, axial velocities and pressure radial distributions (see Fig. 6) at four sections after the swirl element expressed in the pipe radius. The azimuthal velocity has a close profile as a Rankine vortex. The centrifugal force on the fluid, acting towards the wall, is the reason behind the pressure drop in the centre. In addition, we can easily see that the pressure increases with the increase of the azimuthal velocity. The axial velocity profile shows the existence of a reverse flow behind the swirl element, a phenomenon which characterizes swirling flows in general.

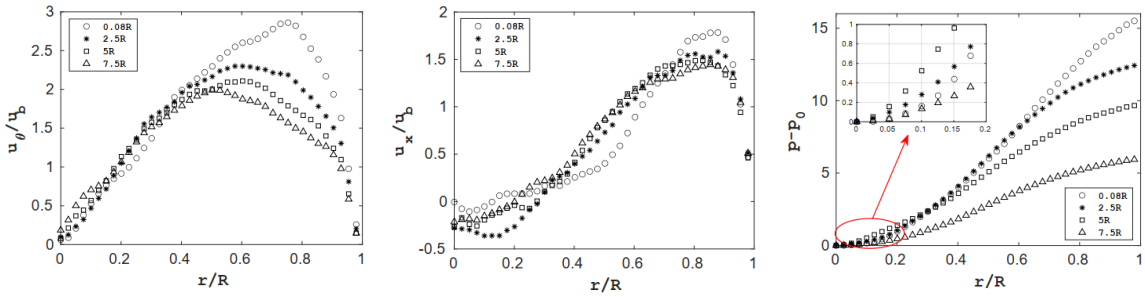

Fig. 6: The radial distribution of the azimuthal and axial velocities and pressure

To characterize the strength of the swirling flow, we introduce the classical swirl number S defined as the ratio of the axial flux of the angular momentum to the axial flux of the axial bulk momentum:

$$S = \frac{\int \rho r u w dA}{R \int \rho u_b^2 dA} \qquad (1)$$

where u_b is the bulk velocity, u is the axial velocity, w is the angular velocity and A is the pipe section.

Fig. 7 represents the variation of the swirl number along the pipe. It is higher at the bottom part of the swirl element and then it decreases following the equation concluded experimentally by Dirkzwager [5]:

$$S(x) = S_0 e^{-C_{ds}(x-x_0)/D} \qquad (2)$$

where S0 is the swirl number at the reference point x0 right after the swirl element, D is the separator diameter and Cds is the swirl decay coefficient depending on Reynolds number, the roughness of the pipe and the swirl intensity.

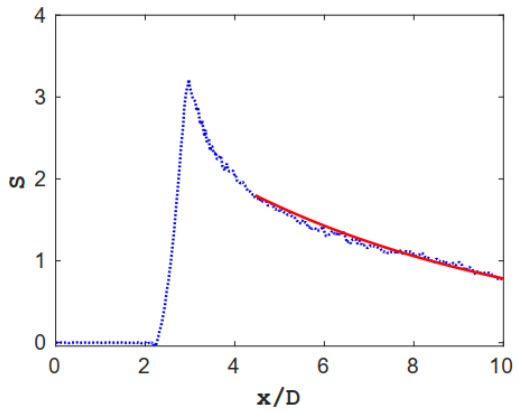

Fig. 7: The swirl number along the separator. The red line represents eq. 2 for Cds=0.15.

The effect of the Reynolds number and the flow split which is defined as the ratio between the pick-up flow rate over the inlet flow rate is also studied.

1.5.2. Two-phase flow in the separator

Numerical simulations of two-phase flows in the separator are carried out using the hybrid approach LT/VoF allowing to transform accumulated bubbles from the Lagrangian framework to form a gas core and solve it using VoF. In Fig. 8, the bubbles are in blue color and the gas core interface is presented in red.

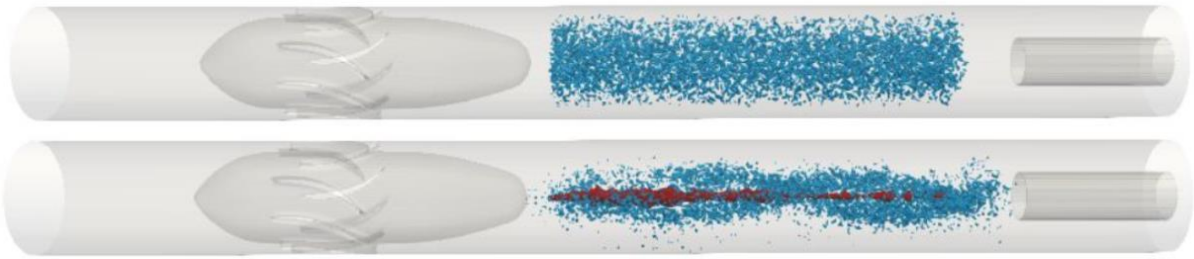

Fig. 8: Two-phase flow simulation using hybrid LT/VoF

By tracking four random bubbles during their motion using the Lagrangian Tracking, we can get their trajectories plotted in Fig. 9. A quasi- spiral shape is observed where the radial position of theses bubbles oscillates around the pipe centre (0.0). Both the migration and capture can be distinguished through characteristic times when the bubble reaches the pipe centre and when it reaches the separator outlet.

The evaluation of the force balance of a bubble provides a direct comparison between the forces applied on the bubbles namely: Drag, lift and virtual mass. The drag is found to be weaker in front of two other forces which control the migration process. Again, the effect of the

bubble size, the flow Reynolds number and flow split on the bubble migration and capture by the pick-up tube is studied.

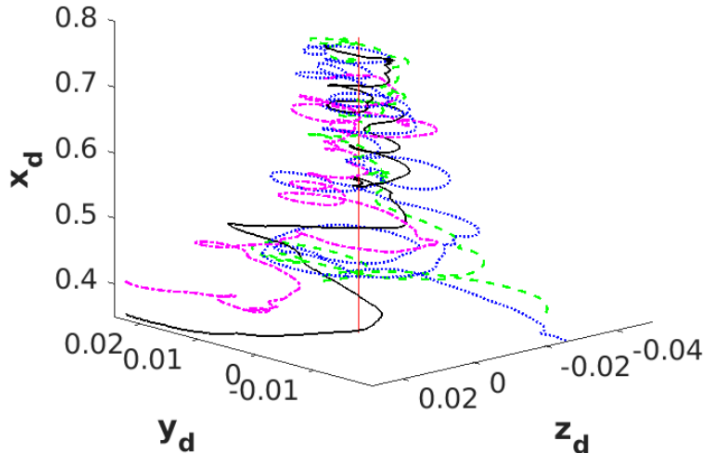

Fig. 9: Trajectories of four bubbles in swirling flow in the separator using LT

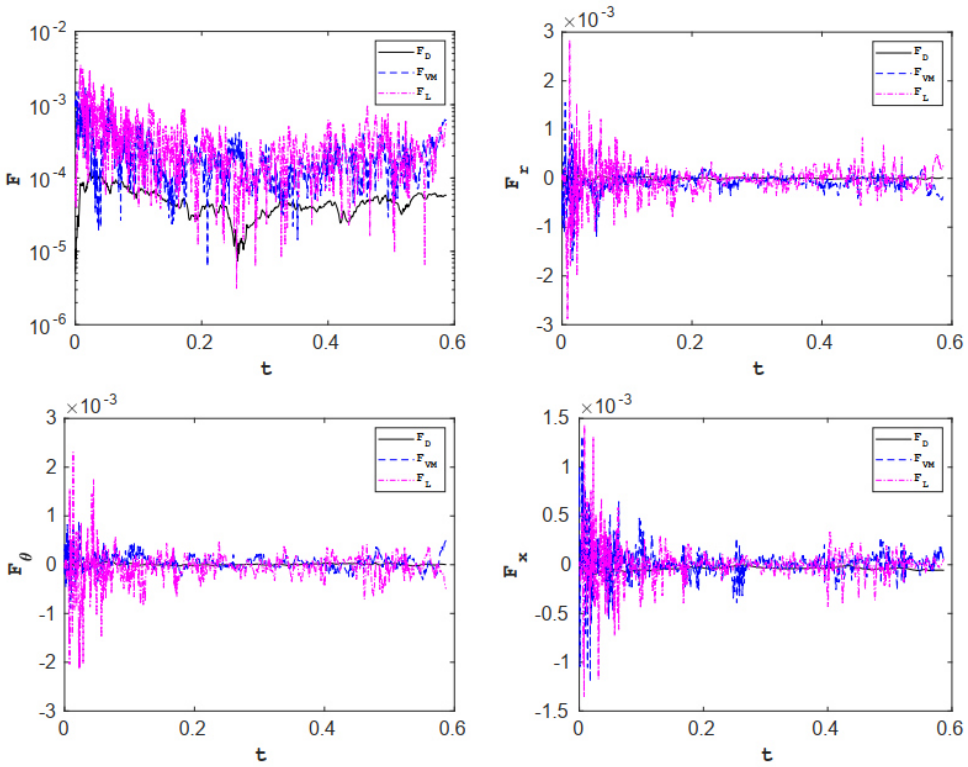

Fig. 10: Forces acting on a bubble in swirling flow in the separator using LT

This project has received funding from the European Union's Horizon 2020 research and innovation programme under the Marie Skłodowska-Curie Grant Agreement No. 764902.

1.6. Conclusion

A hybrid approach is developed and validated to simulate the inline fluid separation process and it consists in coupling LES/IBM, IBM/LT, and LT/VoF as well as updating IBM to be able to simulate complex geometries from a CAD file and introduce the flow straightener with the required condition on the flow split. The simulation of swirling single-phase flow in the separator gives a detailed description of the velocity, pressure and centrifugal force. Then, a simulation of the two-phase flow in the separator is performed using the hybrid LT/VoF and the bubble migration and capture are characterized. The future works consists in comparing the numerical results (the gas core diameter) with the experimental data for the same flow configuration and eventually provide the controller with the physical description of the flow if needed in building a transfer function.

1.7. References

[1] B. Bigot, T. Bonometti, O. Thual, L. Lacaze, A simple immersed boundary method for solid fluid interaction in constant and statified density flows, J. Computers and Fluids, 97:126142, June (2014).

[2] I. Calmet and J. Magnaudet, Large eddy simulation of high schmidt number mass transfer in a turbulent channel flow, Physics of Fluids (1997).

[3] A. Chouippe, E. Climent, D. Legendre, C.Gabillet, Numerical simulations of bubble dispersion in turbulent Taylor Couette flow, Physics of Fluids, 26:043304 (2014).

[4] T.Abadie, J.Aubin, D.Legendre, On the combined effects of the surface tension force calculation and interface advection on spurious currents within Volume of Fluid and Level Set frameworks, Journal of Computational Physics, 297, 611-363 (2015).

[5] Dirkzwager, PhD thesis: A new axial cyclone design for fluid separation, Delft University of Technology (1996).

2. Continuous Casting

2.1. Introduction

Steel casting is one of the most important industrial processes that fills humanity's needs in this material widely used in a lot of technological solutions. Nowadays, the great majority of the operated steel is obtained with continuous casting (CC) technology taking a leading role in the world steel production. Although the continuous casting has been actively used since the 1950s, incessant efforts to improve the efficiency of the entire process and specific crucial parts are being made. One of these crucial parts is the transportation of the highly turbulent liquid metal flow from a tundish to a casting mold through a submerged entry nozzle (SEN) since it is well-known that various destructive phenomena occurring in the mold, such as excessively strong double-rolls or involving slag particles, etc., are responsible for the significant reduction of the product quality. To make such a sensitive process more stable, several control

This project has received funding from the European Union's Horizon 2020 research and innovation programme under the Marie Skłodowska-Curie Grant Agreement No. 764902.

tools, including in particular the electromagnetic brake (EMBr), are used. The application of the electromagnetic brake becomes possible due to the electrically conductive nature of the liquid metal, and therefore the interaction between the magnetic field (created by the EMBr) and the fluid results in the contributing Lorentz force, referring researchers to the magnetohydrodynamic (MHD) flows. Studying the MHD flows is always associated with notorious difficulties, especially in the experiments. Given the extremely high temperature of the liquid steel, the operation difficulty of the experimental setup related to the thermal control rapidly expands. That compels researchers to use cold liquid metals, such as GaInSn. In addition, one has to deal with non-transparency properties of the liquid metal, performing quite a challenging task to measure the inner flow structures which are not visible to standard measurement equipment e.g. particle image velocimetry. In numerical MHD, these issues do not present such a challenge.

The vast majority of results presented in the literature describe the flow in the casting mold only consisting of fully electrically insulated walls without taking into account the conductive solidifying shell. Such rare use of conductive walls is associated with various difficulties preventing in-deep research. In the experiments, complexities are associated with manufacture of walls with different conductivity and frequent reassembling of the mold. In the simulations, one has to take into account the electrical potential distribution not only in the fluid but in the conductive walls as well, and therefore the advanced numerical solver has to be created. To summarize, the presented explicit research gap has to be thoroughly analyzed, and thus the effect of conductive walls on the various aspects of the flow in the casting mold is numerically investigated.

2.2. Numerical model

An incompressible single-phase electrically conductive fluid (reproducing the liquid metal properties) is considered. The fluid is subjected to the external constant non-uniform magnetic field resulting in the appearance of the contributing Lorentz force. Thus, one can formulate the governing equations as:

$$\begin{gathered}\nabla \cdot u = 0 \\ \frac{\partial \mathrm{u}}{\partial \mathrm{t}} + (\mathrm{u}\cdot\nabla)\mathrm{u} = -\frac{1}{\rho}\nabla \mathrm{p} + \nu\nabla^2\,\mathrm{u} + \underbrace{\frac{1}{\rho}(\mathrm{j}\times \mathrm{B})}_{\mathrm{F^L}} \\ \nabla^2\phi = \nabla\cdot(u\times B) \\ \mathrm{j} = \sigma(-\nabla\phi + \mathrm{u}\times \mathrm{B})\end{gathered} \tag{3}$$

where $\boldsymbol{u}$ is velocity, p is pressure, ν is the kinematic viscosity, ρ is density, $\boldsymbol{j}$ is the current density, and $\boldsymbol{B}$ is the constant imposed magnetic field, ϕ is the electric potential, and $\boldsymbol{F^L}$ is the Lorentz force.

The liquid metal flow in the continuous casting mold is expected to be highly turbulent (Re = 32000), and therefore special attention should be devoted to the correct turbulence prediction. In the present study, the Large Eddy Simulation (LES) method has been chosen to perform

This project has received funding from the European Union's Horizon 2020 research and innovation programme under the Marie Skłodowska-Curie Grant Agreement No. 764902.

the turbulence modelling due to the fact that LES is still a very accurate but computationally cheaper method, compared to the Direct Numerical Simulation (DNS) method. The dynamics Smagorinsky sub-grid scale (SGS) model is used to close the system of equations. To model electrically conductive walls, we use our recently developed conjugate MHD method. The conjugate MHD method is generally focused on splitting fluid and conductive walls into different computation domains and resolve the electric potential equation for each domain separately. To carry out the simulations, we used our own finite-volume MHD solver based on the open-source library OpenFOAM.

2.3. Mini-LIMMCAST setup

For the present study, the geometry used for the numerical simulations is based on the most recent version of the laboratory-scaled mold of a continuous caster at Mini-LIMMCAST (Liquid Metal Model for Continuous Casting) facility located at Helmholtz-Zentrum Dresden-Rossendorf (HZDR). The geometric characteristics of the mold are described in the same scales as in the experiment: The distance from the outlet to the meniscus $L = 0.612$ m, the width of the mold K = 0.3 m, the SEN immersion depth him = 0.035 m, the half-thickness of the mold $D = 0.017$ m and the conductive walls thickness $d_w = 5 \cdot 10^{-4}$ m.

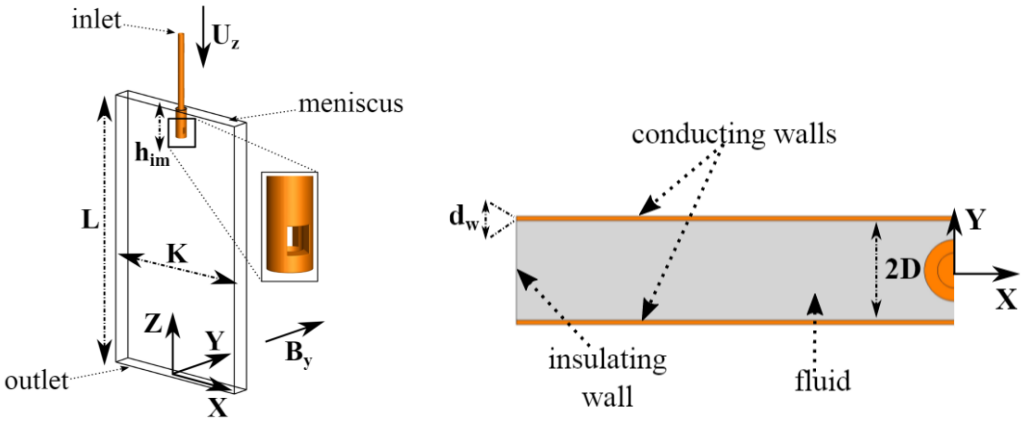

Fig. 11: Sketch of the numerical setup. On the left – a side view of the entire mold. On the right – a top view of the left-half part of the mold.

The constant flow rate obtained from the experiment $Q_{flow} = 7.17 \times 10^{-5} m^3/s$ has been imposed at the inlet, and the zero-pressure boundary condition has been imposed at the outlet. The no-slip velocity boundary conditions have been applied to all walls. It should be noted that the meniscus needs special treatment by applying the slip-free velocity boundary condition. Another key point is the correct application of the external magnetic field. The most contributing component of the magnetic field ($\boldsymbol{B}_y$) has been experimentally measured along the z-axis and later interpolated for the numerical mesh.

Considering the strength of the magnetic field and the wall conductivity ratio, simulations can be divided into two groups. The first group (I) of simulations, aimed at validation with the experiment, has been performed by keeping the wall conductivity ratio $C_d = (\sigma_{wall} d_w)/(\sigma_{liquid} D) = 0$ for all walls (i.e. fully insulated case, $\partial\phi/\partial n = 0$ at the walls) and changing the

strength of the EMBr in the range of $0 \leq I \leq 375\,A$. The second group of simulations (II), aimed directly at studying the conjugate MHD effect, has been conducted by varying the wall conductivity ratio for two wide walls perpendicular to the magnetic field (i.e. Hartmann walls) in the range of $0.025 \leq C_d \leq 5$. The EMBr strength remained as $I = 225\,A$ for all conjugate MHD cases as well as the insulated nature of two narrow walls parallel to the magnetic field (i.e. Shercliff walls). Additionally, the extreme case, such as the fully conductive case ($C_d \rightarrow \infty$, $\phi = 0$ V at the Hartmann walls) has been considered as well.

2.4. Results

We start the analysis by performing the simulations from group I and validating the numerical results against the existing experiment. The exact comparison between the simulations and experiment (four different EMBr strengths, $C_d = 0$) is presented in Fig. 12, namely time-averaged velocity profiles in different cross-sections. In the experiments, velocity measurements have been done by Ultrasound Doppler Velocimetry (UDV) with an array of 10 ultrasound transducers on the upper part of the narrow wall. One should take into account that UDV can measure the velocity along the entire length of the beam but only the component in the axial direction of each transducer (the x-component for the present case) and the velocities are spatially averaged depending on the diameter of the ultrasound beam (which is 8 mm for the present setup). The further application of the developing tomography sensors will significantly expand the validation capabilities. These sensors are being currently developed by TOMOCON participants and are expected to be delivered in the near future.

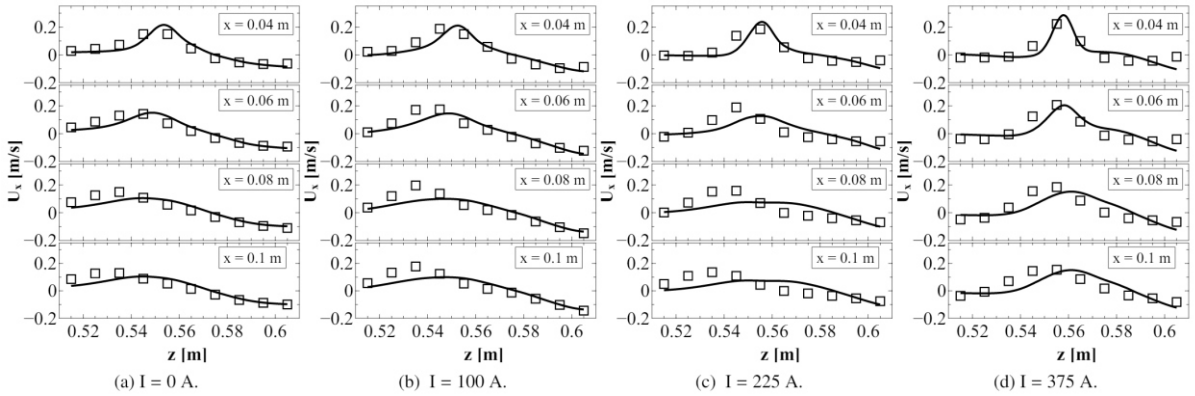

Fig. 12: The horizontal (x-direction) time and spatial averaged velocity profiles at $0 \leq I \leq 375$ A and $C_d = 0$. The following indication is used: line - the present numerical study, symbols - the experimental results obtained by HZDR.

As it can be seen, the numerical simulations properly predict the magnetic field influence and match the experiments with a very good agreement. Next, in order to examine the effects of the conductive walls, we have performed the numerical simulations from group II with the variable wall conductivity parameter and the constant EMBr strength. The moderate value of EMBr $I = 225$ A has been used for the second group of simulations in view of provision the well-balanced influence of the magnetic field on the flow. The analysis starts from the neutral case

where the classical unaffected double-roll flow structure as a result of jets motion, with two smaller upper rolls and two bigger lower rolls, can be observed (Fig. 13a). Activation of the magnetic field (Fig. 13b) significantly lifts the lower rolls towards the meniscus and Shercliff walls, while the upper rolls are shifted towards the SEN. For $C_d = 0.05$, the upper and lower vortexes surprisingly represent almost the symmetrical distribution against each other. Their shape and position are remarkably changed, rolls are elongated in the horizontal direction and squeezed in the vertical direction. With a further increase of the wall conductivity (Fig. 13d), the gradual squeezing of vortexes in both directions is observed. Rolls tend to cluster predominantly around the port. However, after reaching $C_d = 0.5$ (Fig. 13e), only bottom rolls remain active, while the top rolls are almost eliminated. Finally, for $C_d \to \infty$ (Fig. 13f), the double-roll flow structure is totally suppressed by the magnetic field, replaced by the well-established relatively simple pattern.

The other area representing the research interest for the continuous casting flow is the meniscus zone. It is well known that rolls with excessively high velocities can potentially involve the slag layer from the free surface into the downstream flow, provoking unnecessary problems for the entire process. Based on that, the influence of the conductive walls on the meniscus velocity should be analyzed thoroughly. The distribution of the horizontal (x-component) time-averaged velocity at the meniscus surface is presented in Fig. 14. As it can be seen from the contours, the increase of the wall conductivity causes the significant transition in a flow direction. Initially, for the non-MHD case (Fig. 14a), the flow is directed towards the SEN. By activating the magnetic field and increasing the wall conductivity, the flow velocity gradually reduces until the flow direction is reversed at $C_d = 0.5$, Fig. 14e. A further increase of the wall conductivity results in stronger reverse velocities, i.e. more intensive fluid motion towards the Shercliff walls, Fig. 14f. Such behavior will directly affect the slag formation at the meniscus, in particular, enlarge bulk clustering near the Shercliff walls.

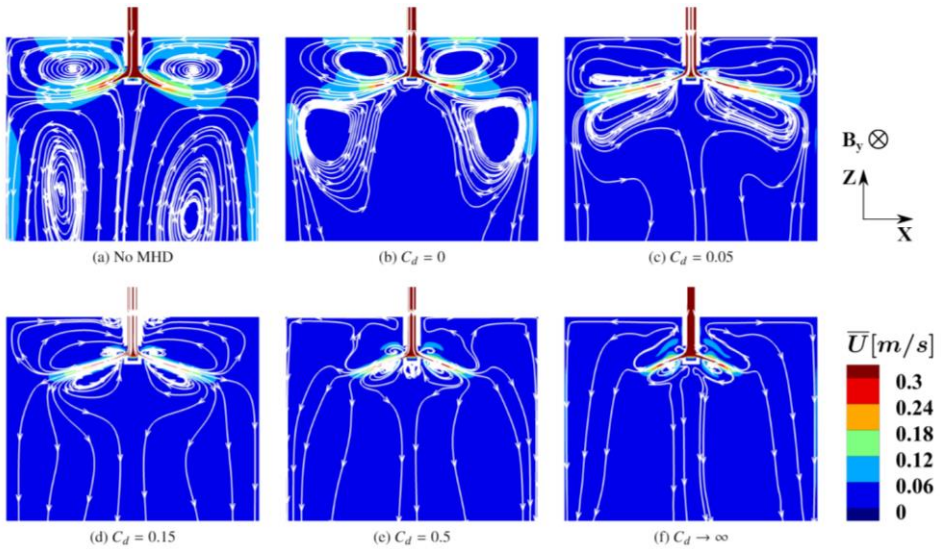

Fig. 13: The time-averaged velocity magnitude contours with time-averaged velocity streamlines in the vertical ($y = 0$ m) cross-section (upper half of the mold) for the range of EMBr strength and the specific wall conductivity ration of $C_d = 0$

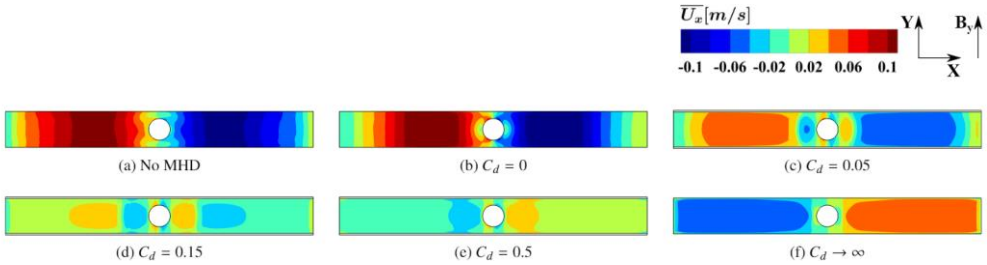

Fig. 14: The time-averaged horizontal velocity contours at the meniscus for the range of C_d parameters and the specific EMBr strength of $I = 225$ A.

2.5. Conclusion

The comprehensive numerical study of the wall conductivity influence on the turbulent liquid metal flow in the casting mold Mini-LIMMCAST, subjected to the imposed magnetic field, has been presented. The advanced in-house solver, based on open-source code OpenFOAM has been used. Considering the fully insulated walls, the validation with the experimental data (obtained via UDV sensors by HZDR) has been performed and a good agreement has been achieved. However, it is expected that the new generation of tomography sensors will provide a better resolution of the continuous casting flow pattern. Next, the extensive range of the arbitrary wall conductivity ratio $0.025 \leq C_d \leq$ has been thoroughly examined. It was shown that an increase of C_d resulted in the dramatic reorganization of the double-roll flow structure: Suppression of flow oscillations, reduction of the rolls vertical size, and rolls stretching in the horizontal direction. In addition, we have demonstrated that the meniscus velocities are highly sensitive to the presence of conductive walls, reaching the minimum values in the range of $0.2 \leq C_d \leq 1$ and swapping the flow direction with a further increase of C_d.

3. Microwave Drying

3.1. Introduction

Microwave drying is an emerging technology in the industry for batch and continuous processing due to the possibility of volumetric and selective heating. Interaction of high-power microwaves for drying materials with certain moisture content results in significant energy and time saving compared to conventional, convective, and radiative heating. In the studied drying application, the objective is to dry polymer foams uniformly with the final target to keep the moisture at a certain level inside the polymer foam at the end of the drying process.

Designing an advanced tomography-assisted controller for this process is the novel idea of this research to achieve the mentioned process goals. Two sensors, microwave tomography (MWT) and electrical capacitance tomography (ECT), are designed for this process to estimate the input and output material moisture, respectively. The schematic of the tomography-controlled microwave drying is depicted in Fig. 15. The system is equipped with a conveyor belt to enable a continuous process. The MWT is installed at the inlet of the heating system, while

ECT is installed at the outlet to estimate the moisture level in the polymer foam and feedback the measurements to the control unit.

One of the requirements in developing a control system for this process is a mathematical model that simulates the process behavior with high accuracy. In the following sections, the procedure for deriving such a model is explained.

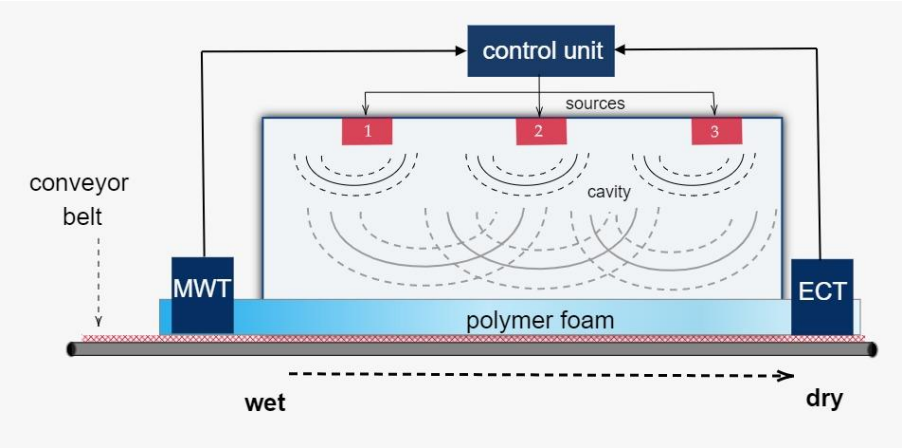

Fig. 15: A schematic of the tomography-controlled microwave drying

3.2. Process modelling

Process models are used for several tasks, such as simulations and control design. There are various techniques to model a process. One approach is first-principle modelling, in which the physics and mathematics behind the process are entirely known. Therefore, a model using these principles can be developed. The second technique is called data-driven modelling or system identification. In this technique, there is no knowledge of the details of the system. However, there is measured data available, and using these data, a model can be derived for the process.

In this project, first, a model of the microwave drying process was developed based on the knowledge of the heat and mass transfer in a microwave drying process. System identification was adopted as the second modelling approach of modelling and required collecting input-output data from the system.

3.2.1. First-principles modelling

The analytical model was derived based on a Luikov model of heat and moisture transfer, which consists of a pair of coupled parabolic PDEs [1]. The derived model was modified according to our process specifications to include the effect of microwave heating. The equations describing the heat and mass transfer in the foam inside the microwave oven are

$$\rho \frac{\partial}{\partial t}\left[\frac{M}{100}\right] = \vec{\nabla} \cdot \left[\left(\frac{k_m \delta}{c_m}\right) \nabla T + \frac{k_m}{100 c_m} \vec{\nabla} M\right], \tag{4}$$

$$\rho c_q \frac{\partial T}{\partial t} = \vec{\nabla} \cdot \left[\left(k_q + \frac{\mu \lambda k_m \delta}{c_m} \right) \nabla T + \frac{\mu \lambda k_m}{100 c_m} \vec{\nabla} M \right] + P_{mw}^n u, \tag{5}$$

where M is the dry-basis moisture content percentage, T is the temperature, k_m is the moisture conductivity, k_q is the thermal conductivity of the moist material, c_m is the moisture capacity, c_q is the heat capacity, δ is the thermal gradient coefficient, ρ is the density, λ is the latent heat of vaporization and μ is the ratio of vapor diffusion coefficient to coefficient of total moisture diffusion. The last term in Eq. (5) describes the effect of microwave heating. The boundary conditions for the PDEs (4)-(5) are described by

$$-k_q \frac{\partial T}{\partial n} = h_q (T - T_g) + \frac{(1-\mu)\lambda h_m}{100 c_m} (M - M_g), \tag{6}$$

$$\frac{-k_m}{100 c_m} \frac{\partial M}{\partial n} = \left(\frac{k_m \delta}{c_m} \right) \frac{\partial T}{\partial n} + \frac{h_m}{100 c_m} (M - M_g), \tag{7}$$

where h_q is the convective heat transfer coefficient, h_m is the convective mass transfer coefficient, M_g is the bulk gas moisture content and T_g is the bulk gas temperature. Equations (4)-(7) are discretized and solved numerically in 2D/3D using Finite Element Method (FEM). Computing the microwave heating power P_{mw}^n requires the information of the electric field and this information is calculated using COMSOL Multiphysics.

The FEM solution was implemented in MATLAB software and is well integrated into SIMULINK for a virtual demonstration. A smaller foam size than the actual size of the foam in the drying process was used in this simulation to reduce the computational time. Additionally, only 6 out of 18 microwave sources and a total of 18 kW were considered. Since not all the parameters related to the polymer foam were available, the wood parameters taken from the literature were used. The moisture content removal over time is shown in Fig. 16. Also, the average moisture and temperature of the sample are illustrated in Fig. 17. As seen, the average moisture reduces over time, and the average temperature increases to a steady-state value and remains constant. Since the wood parameters are used in this simulation, the average moisture changes slowly, although the temperature is high. However, using the foam parameters will result in a faster change in the material moisture.

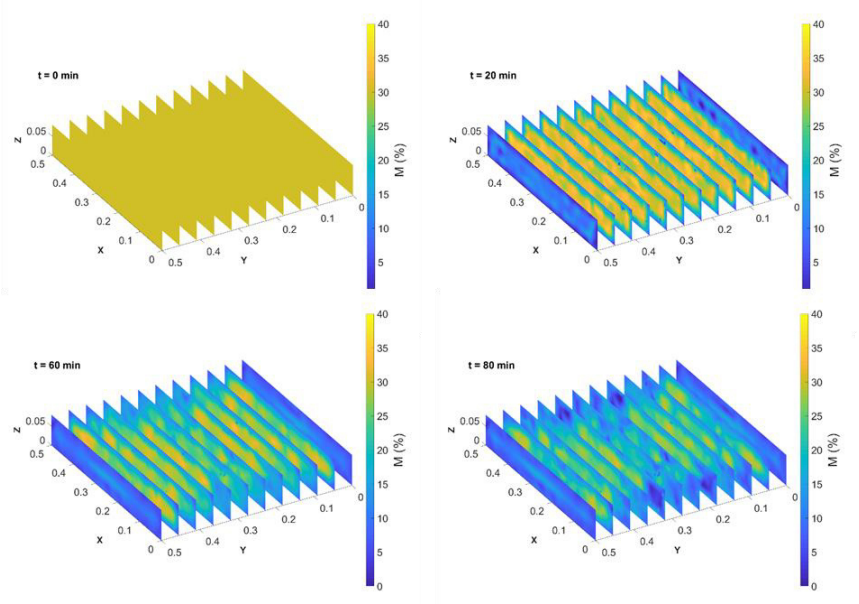

Fig. 16: Moisture distribution of the sample foam over time

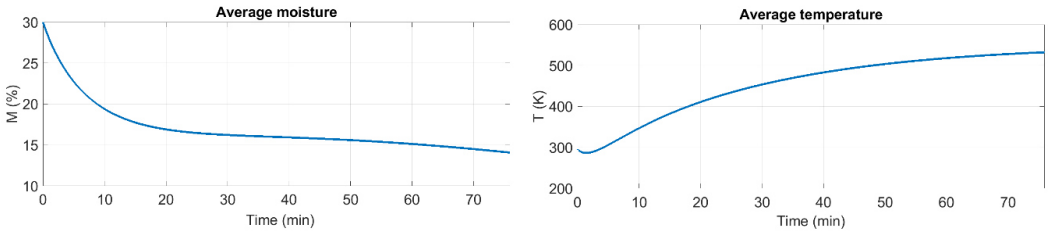

Fig. 17: The average moisture and temperature of the whole sample over time

The derived model with the first-principal approach was used to design an LQR controller for the microwave drying process [2]. This model can be later modified by using the foam parameters and be validated with some modifications through the experiments conducted to collect input-output data for the system identification approach.

3.2.2. System identification

The second approach in modelling is system identification. In this approach, the system input, which is the input power to the microwave sources, is determined based on some specifics and applied to the system. Meanwhile, the corresponding system output, the dried foam moisture, is measured and collected by the ECT sensor. It is worth mentioning that the ECT sensor estimates the permittivity distribution of the material, which is strongly correlated with the material moisture. The collected permittivity distribution can later be converted to the moisture information via a calibration map. The efficiency of the ECT sensor in estimating the moisture distribution of a moving polymer foam was already studied and proven [3].

In our experiments for collecting input-output data, several boards of foam with a length of 1.5 m were moisturized and sent to the microwave oven right after each other to simulate a continuous process. After passing through the microwave oven, the input foams entered the ECT sensor at the end of the process. The belt speed was fixed at 40 cm/min, so it took 1129 sec for any point of the foam to travel from the entrance of the microwave oven until the middle of the ECT sensor. Figure 18 shows the timeline and the foams sequence while passing through the oven. As can be seen, after any change in the input power or the input foam, there will be a time delay before measuring the output.

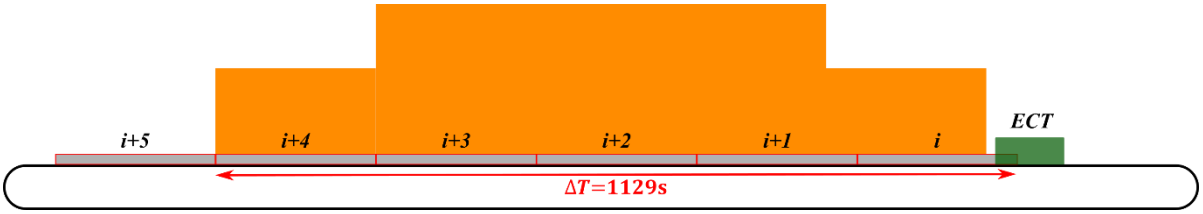

Fig. 18: Foams sequence in input-output data collection for the system identification

The goal was deriving a linear dynamic model, so input power was chosen as the step signal with increasing and decreasing amplitude, PRBS (pseudo-random binary sequence) signal, and APRBS signal (amplitude modulated pseudo-random binary sequence). The sample time, pulse width, and the range of input change were determined based on the specifics of the process. To simplify the problem, first, the same input was applied to all microwave sources, and the average permittivity estimated by the ECT sensor was collected. This way, a single-input single-output (SISO) model could be calculated. In the next step, individual inputs were given to each three microwave sources. This way, we reduced the number of independent sources from 18 to 6 and kept the possibility of designing a multi-input multi-output (MIMO) model.

Different data sets were collected, and one of them was used in the MATLAB system identification toolbox to estimate a state-space model. The other datasets were employed to validate the accuracy of the estimated model. The state-space equations for the acquired SISO model are as follows:

$$x(k+1) = Ax(k) + Bu(k), \tag{8}$$

$$y(k) = Cx(k) + Du(k), \tag{9}$$

where the matrices, A, B, C, and D are obtained from the MATLAB toolbox, x is the state vector with eight elements, u is the system input with two elements: The first one is the control variable which is the synchronized power percentage for all microwave sources ($u_1 = P \in [0,100]$), and the second input, u_2, is the input foam moisture which is considered as the input disturbance to the system. This input foam moisture was collected by measuring the average weight of each board of foam using a scale before sending them into the microwave oven.

The derived model response compared to the training data set is shown in Fig. 19. The upper subfigure here shows the chosen input signal in this experiment which is a PRBS signal. The bottom subfigure is the permittivity change percentage of the output material on a wet basis over time. The ECT sensor estimates the permittivity change compared to the permittivity of the dry foam. Having this permittivity change, the variable $\Delta\epsilon_w$, which is correlated with the moisture percentage on a wet basis, can be easily calculated as in [3]. Since the foams were wet before sending them to the oven, they have some initial moisture and, therefore, a high value of $\Delta\epsilon_w$, which got reduced by increasing the power over time.

Two other datasets were used to validate the derived model. In the first dataset, a step signal with increasing and decreasing amplitude was applied to the system, while in the second data set, an APRBS signal was chosen as the system input. Figure 20 shows the model verification with both mentioned datasets. As can be seen, with different input patterns to the microwave oven, the derived model can still calculate the system output with reasonable accuracy. In Fig. 19 and Fig. 20, the accuracy of the model response compared to the actual measurements is indicated by a fit parameter over the bottom subfigure. The fit is calculated using the NMSE (normalized mean squared error) cost function in which the -Inf is an indication of a bad fit, while 1 is the perfect fit. As can be seen for the training data set, it is 97.5 % which is very near to the perfect fit, and the fit for the validation datasets is 90.78 % in the case of APRBS signal and 68.74 % in the case of step signal. Considering that we modelled a highly complex non-linear system using a linear model, this is a very acceptable fit. The results of the system identification of the microwave drying using the ECT sensor data will be submitted to the TOMOCON special issue of MDPI sensors [4].

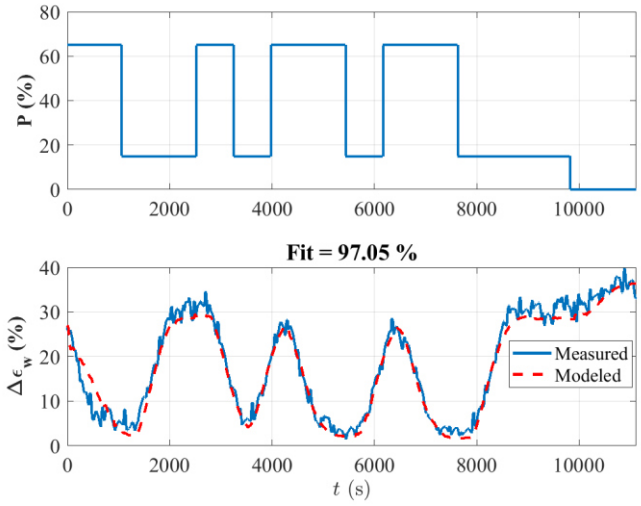

Fig. 19: The derived model simulation results using the training dataset

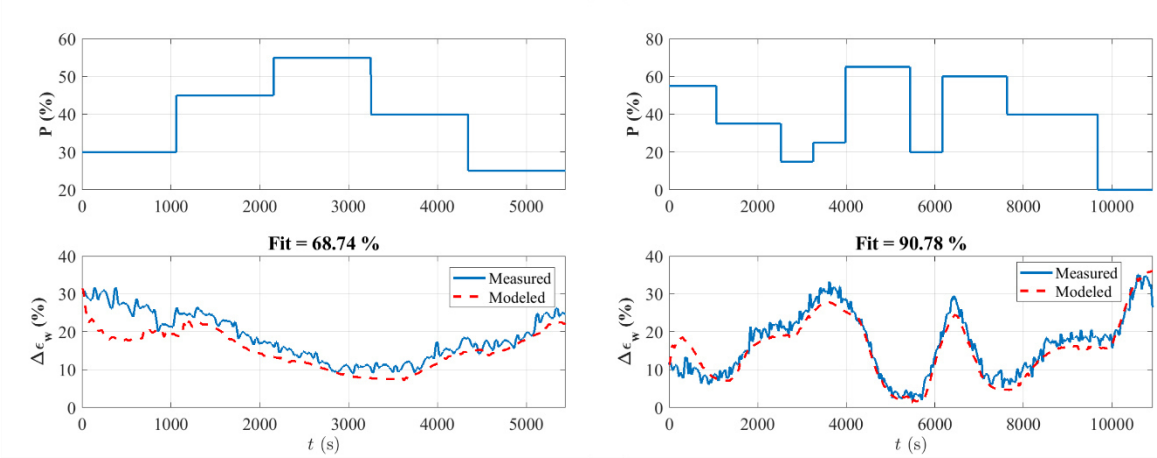

Fig. 20: The derived model simulation results using the validation datasets

3.3. Conclusion

The microwave drying process was modelled using two different approaches. The first approach was based on the physics behind the process, while the second approach was black-box modelling using the system identification approach. The first approach was only validated through simulations, and it was used to design an LQR controller for the microwave drying process. This model will be validated using the actual measurements in the future. However, the second approach was validated using different datasets collected via the ECT sensor measurements. The model derived using the second approach was employed to design the control system for the final demonstration.

3.4. References

[1] A. V. Luikov, Heat and mass transfer in capillary-porous bodies, Advances in Heat Transfer, Vol. 1, Elsevier, 123-184 (1964).

[2] M. Hosseini, A. Kaasinen, G. Link, T. Lähivaara and M. Vauhkonen, LQR Control of Moisture Distribution in Microwave Drying Process Based on a Finite Element Model of Parabolic PDEs, IFAC-PapersOnLine, 53(2), 11470-11476 (2020).

[3] M. Hosseini, A. Kaasinen, G. Link, T. Lähivaara and M. Vauhkonen, Electrical Capacitance Tomography to Measure Moisture Distribution of Polymer Foam in a Microwave Drying Process, IEEE Sensors Journal, doi: 10.1109/JSEN.2021.3085762.

[4] M. Hosseini, A. Kaasinen, G. Link, T. Lähivaara and M. Vauhkonen, System identification of microwave drying process of polymer foams using electrical capacitance tomography, Unpublished.

This project has received funding from the European Union's Horizon 2020 research and innovation programme under the Marie Skłodowska-Curie Grant Agreement No. 764902.

4. Batch Crystallization

4.1. Abstract

In this numerical study, experimental data of a calcium carbonate crystallization process is utilized to develop a mathematical framework for analyzing the spatial distribution of the solid particles in the crystallizer. The proposed mathematical formulation pre-calculates the CFD input data through parameter estimation and data fitting to the Rosin-Rammler (R-R) particle size distribution equation. The 3D CFD simulations of the mixing hydrodynamics are used to estimate the total energy dissipation, ϵ; then, utilizes ϵ to estimate the mass fraction of particles. The CFD model is validated based on experiment torque measurement.

A possibility of validation and comparison of the simulated species transport in the flow field by experimental data of the electrical resistance tomography (ERT) and ultrasound tomography (UST) is under further investigation.

4.2. Objectives

The current CFD investigation pursues three main objectives, namely:

(a) Developing a set of user-defined subroutines in the 3D simulation to formulate the size classes and spatial distributions by coupling the Rosin-Rammler equation and total dissipation energy (effects of mixing).

(b) Calcium carbonate precipitation in the experimental reactor is opaque; hence, simulating the crystallization reaction and distribution of species in the flow field is beneficial for studying the behavior of the system at different operating conditions.

(c) Proving a CFD framework that can be used in parallel with ERT and UST.

4.3. Approach

Experimental particle size distribution curves are divided into an adequate number of discrete size intervals and then fitted to the R-R exponential equation. The main parameters of the R-R equation (spread and size factors) are correlated to the total energy dissipation rate (ϵ). The $k-\omega$ SST and the Scale Adaptive Simulation (SAS) turbulence models are used to calculate the turbulent flow field of the computational domain.

The final equations for each size class are implemented in the CFD solver ANSYS Fluent as scalar transport equations in a form of user-defined subroutines. The subroutines are coupled to the single-phase species transport equation of the crystallization process. Mass fraction is evaluated in cells that contain solid particles as a result of the chemical reaction.

Additionally, momentum source term subroutines are used to visualize the effects of feed addition during the single-phase and constant-volume simulation. Temporal species distributions are constructed during the CFD simulation that can be further analyzed with UST-ERT.

This project has received funding from the European Union's Horizon 2020 research and innovation programme under the Marie Skłodowska-Curie Grant Agreement No. 764902.

4.4. Introduction

Simulation and analysis of particle size distribution (PSD) of a crystallization process with computational fluid dynamics (CFD) are mostly limited to population balance modelling (PBM). Utilizing PBM in this context has significant drawbacks, such as consuming intensive computing power (high computational cost) and a great number of kernels and parameters (nucleation, aggregation, breakage, etc.); these drawbacks limit the practicability of the method for fast-kinetic systems.

In this study, a mathematical formulation based on the Rosin-Rammler distribution equation is proposed to pre-calculate CFD input data through parameter estimation and data fitting. The user-defined subroutines contain actual information from experiments that can be further developed to visualize the average particle concentration and distribution in a stirred tank reactor.

The current approach is made possible by imposing a series of assumptions: (i.) Crystallization reaction and particle formation are instantaneous, (ii.) Particles are moving with the flow due to small ranges of the Stokes' number, (iii.) Liquid height increase due to reagent addition is negligible and the effects of volume can be modelled as separate simulations.

4.5. Materials and methods

4.5.1. Batch crystallization experimental set-up

The experimental setup consists of a plexiglass unbaffled crystallizer of a diameter of 190 mm equipped with an overhead stirrer (Heidolph Instruments GmbH). The agitation speed of a six-blade Rushton turbine (diameter = 70 mm) varies in the range of 100 RPM to 300 RPM during the experiments. The calcium carbonate crystallization process considered in the present work is an instantaneous and homogeneous liquid reaction that results in the precipitation of micron-sized solid particles. In the system under investigation, aqueous CO_3^{2-} as the reagent solution flows through an inlet pipe (diameter: 2 mm) into the crystallizer containing calcium chloride. The chemical reaction governing the crystallization of calcium carbonate is presented in Eq. 10:

$$CO_3^{2-}{}_{(aq)} + 2\,Na^{+}{}_{(aq)} + CaCl_{2\,(aq)} \rightarrow CaCO_{3\,(s)} \downarrow + 2\,NaCl_{(aq)} \qquad (10)$$

4.5.2. Process monitoring by ultrasound and electrical tomography systems

The crystallization process that is used for the current numerical analysis is monitored by two tomographic modalities. The ultrasound tomography system consists of a circular ring of 16 transducers and characterizes the medium by measuring the time of flight (TOF) of the sound propagation; the electrical resistance tomography is equipped with a single plane of 16 stainless steel electrodes mounted around the perimeter that measures the electrical current distribution (TOMOCON Deliverable 2.4).

Fig. 21 shows the experimental setup for calcium carbonate crystallization monitoring with UST and ERT systems.

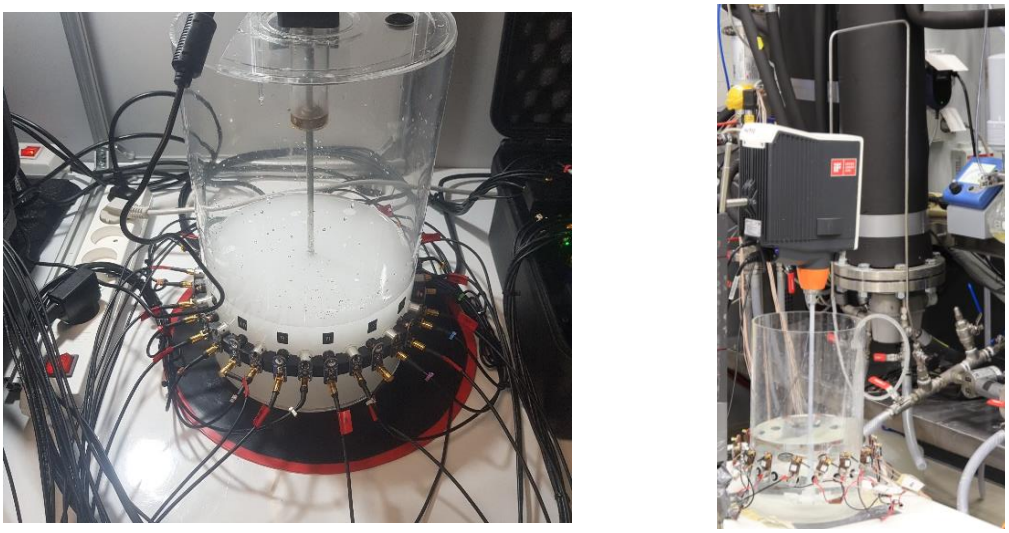

Fig. 21: Experimental setup of the crystallization experiments. Left: Ultrasound tomography. Right: Electrical tomography system.

4.6. Numerical Model

4.6.1. Geometry description and computational mesh

Fig. 22 shows the schematics of the experimental setup, reactor configuration, and the computational mesh that are used to carry out the numerical simulations. The tank lid is closed with a flat cover and is treated as a wall during the analysis, which helps to avoid the formation of air bubbles and stabilizes the numerical simulation.

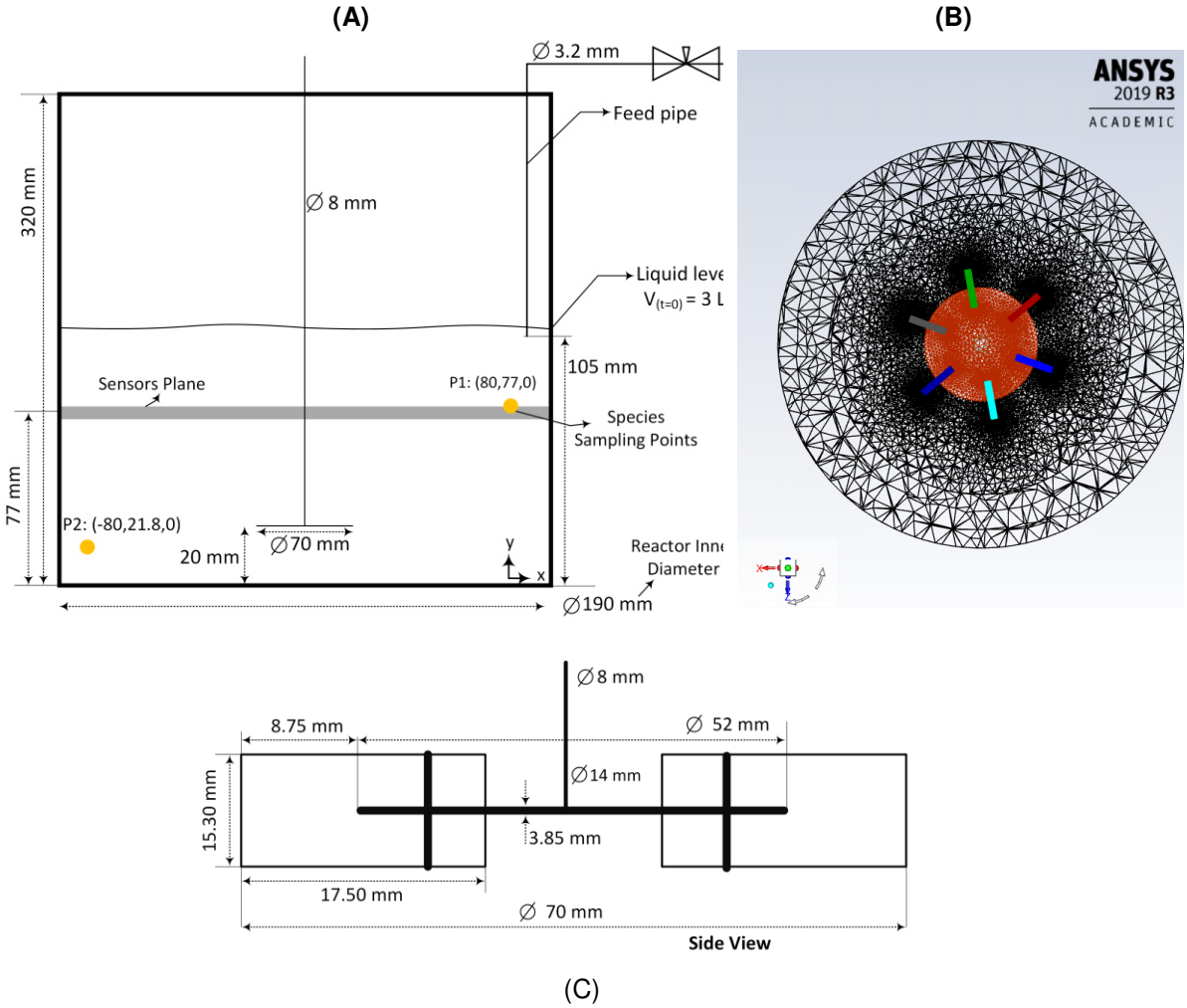

Fig. 22: Schematics of the experimental setup. (A) Dimensions of the experimental reactor and position of the UST-ERT sensors. (B) Bottom view of the computational mesh of the six-bladed Rushton turbine over a cut-plane at the middle of the impeller. (C) Detailed geometry of the blades.

4.6.2. CFD model for mixing hydrodynamics

The 3D geometry and unstructured tetrahedral mesh are generated in ANSYS DesignModeler software (Release 2019-R3). Due to the rotation of the impeller in the flow domain, the computational volume is divided into two cell zones that comprise a stationary (tank) and the rotating impeller region, which are bonded together by an interface layer and modelled using a sliding mesh approach. Sliding mesh is solved transiently and increases the accuracy of the simulation.

Dimensions of the rotating zone are defined to fully resolve the unsteady flow field arising from the movement of the impeller. The height of the rotating region is considered as $H_r = 2w$, where w is the width of the blades equal to $D/5$, while the diameter of the rotating zone is $\mathrm{D_r} = 2\mathrm{D}$; D is the impeller diameter [2].

The angular velocity of the impeller is set at $100\ \mathrm{rpm}\ (1.67\ \mathrm{rps})$ during the entire simulations, resulting in a theoretical tip speed of 0.37 m/s and a Reynolds number of 9,176. To achieve a desirable CFL value of less than one, the time step for the simulations is evaluated as 8×10-3 s, which corresponds to 4.8° angular displacement of the impeller in the computational domain. Additionally, 15 blade passages in the impeller region are modelled to ensure the achievement of a steady-state scenario before modelling the chemical reaction.

Numerical simulations are performed with the finite volume CFD code, ANSYS Fluent solver (Release 2019-R3). Simulations are carried out in double precision mode with the second-order upwind scheme for spatial discretization of the governing equations.

Residual tolerance of the solver is monitored until 10-5 orders of magnitude for convergence, and maximum inner correction iteration for all the governing equations is set at 10. All the simulations are performed in parallel mode on an Intel® Core i7 with 4 CPU processors and a base speed of 3.60 GHz.

To carry out the 3D single-phase flow simulations, the volume of the experimental mixing tank corresponding to 3 l is modelled. The working fluid is water at 25°C. The density and viscosity of the system is constant throughout the simulations at 1000 $\mathrm{kg\,m^{-3}}$ and 0.001 $\mathrm{kg\,m^{-1}s^{-1}}$, respectively.

4.6.3. Turbulence formulation

Steady-state solution of the turbulent flow field obtained based on the Reynolds-Averaged Navier Stokes (RANS) equations with $\mathrm{k-\omega\ SST}$ model. The steady-state solution data is used to perform the unsteady simulations with a combination of the $\mathrm{k-\omega\ SST}$ and Scale Adaptive Simulation (SAS) turbulence models (Table 1).

Table 1: Turbulence models used for the flow simulation in stirred tank reactor

Turbulence model	Classification
k-ω SST	- Unsteady RANS - 2 equation model. - *Before* species transport and user-defined subroutines for PSD modelling.
SAS - Scale Adaptive Simulation	- Unsteady RANS - Additional SAS source term in the turbulence eddy frequency of the k-ω SST model. - - *During* the user-defined subroutines for PSD modelling to enhance the k, ω, and ϵ estimation.

k-***ω*** SST. The Shear Stress Transport (SST) $\mathrm{k-\omega}$ model has been established based on the original k-ω methodology developed by Wilcox [3]. The SST model utilizes the original k-ω model in the sub- and log-layer and progressively switches to the standard $\mathrm{k-\epsilon}$ model in the

wake region of the boundary layer, thus integrates the best elements of the $k-\epsilon$ and the $k-\omega$ models [4].

SAS - Scale Adaptive Simulation. To modify the shortcomings of RANS models in resolving the turbulent spectrum, the von Karman length scale was explicitly introduced into the transport equations of turbulence scale determining factor. The resulting Scale Adaptive Simulation (SAS) turbulence model, which is derived entirely based on RANS arguments, delivers proper RANS performance in stable flow regions, while for flows with transient instabilities, dynamically reduces its turbulent viscosity and adjusts to resolved turbulence structures. The unsteady characteristics of the SAS approach are implemented as a source term (Q_{SAS}) into the transport equation for the turbulence eddy frequency ω of the $k-\omega$ SST model [5].

4.6.4. Establishment of the mathematical model for particle size distribution

Among many particle size distribution functions, the Rosin-Rammler distribution is used in a broad range of applications. The R-R distribution employed in the present numerical analysis assumes (i.) a constant mass density of all particles, (ii.) an exponential relationship exists between particle diameter and mass fraction. In the R-R type function, V, as the mass (or volume) fraction of particles of diameter greater than d (i.e., oversize distribution) can be expressed in the cumulative-volume form [6]:

$$V = e^{-(d/\bar{d})^n} \tag{11}$$

where $\bar{d}$ is the mean diameter or location parameter, n is the spread parameter of the distribution $(n > 0)$ given by:

$$n = \frac{\ln(-\ln V)}{\ln(d/\bar{d})} \tag{12}$$

By fitting the experimental size distribution data of different operating conditions (e.g., several mixing speeds) to the R-R equation, correlations are obtained for parameters of n and $\bar{d}$. To calculate the correlation, the complete range of sizes is divided into an adequate number of discrete size intervals and then fitted to the R-R exponential equation. Size intervals are determined through the experimental particle size distribution (PSD) curves such as cumulative or probability distribution functions. Hence, by conducting the data fitting of PSD for several mixing speeds, R-R parameters are evaluated as a function of total energy dissipation rate (ϵ):

$$\bar{d} = f(\epsilon),\ n = f(\epsilon) \tag{13}$$

The total energy dissipation rate of a batch experiment is estimated experimentally through the total power input (P_τ) and torque measurement (τ) of the stirrer. Moreover, the experimental P_τ is then compared with the approximated CFD simulations, which are obtained by integrating the wall shear stress over the surface of the impeller (Eq. 14) and integrating the local energy dissipation rate over the volume (Eq. 15).

This project has received funding from the European Union's Horizon 2020 research and innovation programme under the Marie Skłodowska-Curie Grant Agreement No. 764902.

$$p_\tau = 2\pi N \int \tau \, d \, A \tag{14}$$

$$p_\tau = \rho \int \epsilon \, d \, v \tag{15}$$

where N is the mixing speed (s^{-1}), A denotes the total surface of the impeller (m^2), ρ is the density of the liquid ($kg\, m^{-3}$) and v is the liquid volume (m^{-3}). In this study, the average energy dissipation of the computational domain is used to develop the R-R correlations and implementation into the CFD solver. PSD functions are implemented as a set of user-defined scalar (UDS) transport equations and user-defined functions (UDF) in the solver. UDFs are solved simultaneously with the species transport equation (reaction Eq. 10) in a transient manner. Coupling the PSD functions with the chemical reaction in the computational domain provides the means to solve the UDS' in the cells that chemical reaction occurs. Fig. 23 shows a graphical representation of the current approach for modelling PSD.

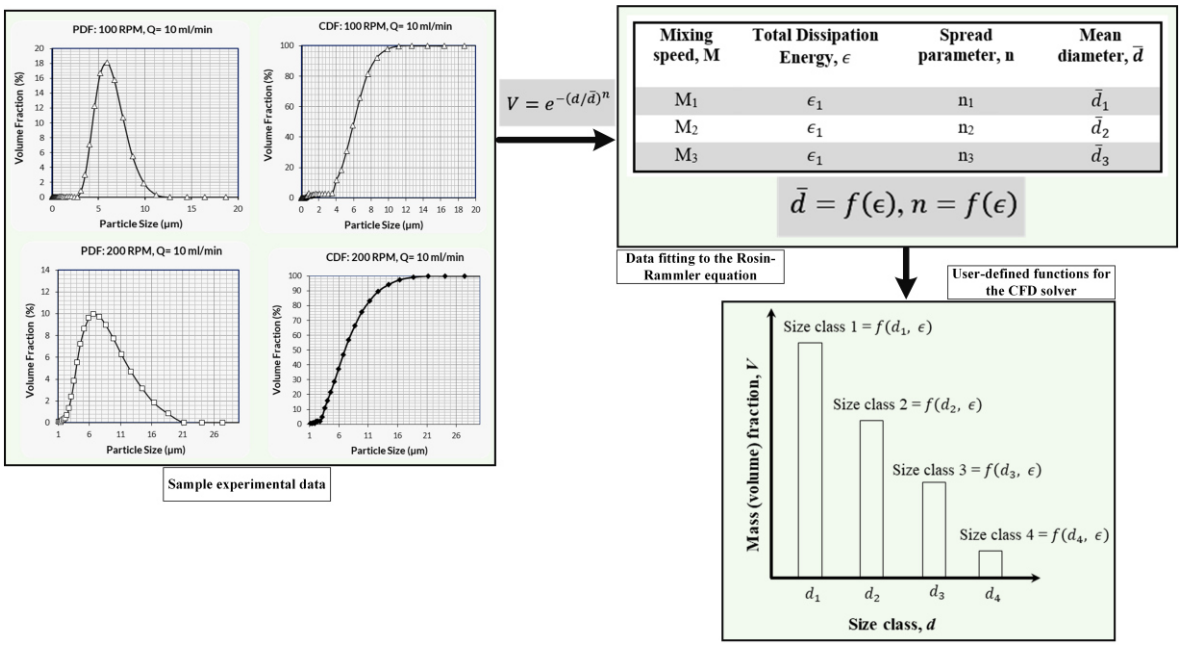

Fig. 23: Graphical representation: Three main steps to transform a particle distribution curve into a Rosin-Rammler-based correlation for CFD simulations. Spread parameter and mean diameter of the R-R equation are correlated to the mean dissipation energy.

4.7. Results and discussions

4.7.1. Grid-independence study

A mesh independence study is conducted to study the effect of grid resolution on the numerical simulation. Simulations are carried out based on the $k-\omega$ SST turbulence model for 4 sets of unstructured tetrahedral grids. As tabulated in Table 2, the results of the mesh study are based on monitoring impeller torque, power number and volume integral of turbulence kinetic energy.

Moreover, as an additional criterion, normal root mean square error (NRMSE) of velocity magnitude (U_{mag}) is evaluated [7]. According to the NRMSE error index, the effect of mesh on numerical simulation and accuracy of the converged solution can be considered insignificant when NRMSE is less than 10 %. Based on the outcomes, grid number 3 is identified as the optimal computational mesh.

Table 2: Results of the mesh study with k−ω SST turbulence model at 100 RPM

Grid #		NRMSE U_{mag}, [—]	Toque [mN. m]	Volume integral of TKE [m^2/s^2] [m^3]×10^{-8}
1	146,157	30.57	0.73	1.38
2	382,041	15.31	1.06	2.71
3	742,990	5.56	1.27	4.64
4	1,249,625	1.30	1.25	5.13

4.7.2. Validation of stirred tank CFD modelling by the experimental torque measurement

The numerical analysis of the present work is validated by comparing the torque measurement from the experiments and estimating the torque on the impeller surface in the CFD model. Table 3 presents the measured torque at three different mixing speeds. An additional approach to validate CFD results could be comparing the simulation with tomographic measurements from the experiments. The validation could be achieved by, for instance, qualitative comparison of the ERT or UST tomographs with planar contours of species distribution of the CFD model (see Fig. 24).

Table 3: Validation of transient simulation based on direct measurement of torque from experiments

#	Mixing Speed (RPM)	Reynolds No. ($\rho D^2 N/\mu$)	Average Torque (mN.m)	
			Simulation	Experiment
1	100	9,176	1.27 ± 0.30	1.39 ± 0.3
2	200	18,352	6.30 ± 1.12	5.53 ± 0.5
3	300	27,528	14.54 ± 1.30	15.80 ± 0.6

4.7.3. Temporal distribution of species in the fluid domain

To analyze the spatio-temporal distribution of calcium carbonate in the stirred tank reactor, a single-phase flow system coupled with species transport is solved in a transient numerical simulation. Chemical species variation in the liquid phase is calculated using a transport equation for each species i in the continuous phase. Reaction Eq. 10 is solved transiently in the computational domain. The crystallization process is conducted at the initial $Ca^{2+}_{(aq)}$ and $CO^{2-}_{3(aq)}$ concentrations of ca. 0.042 $\mathrm{mol\ L^{-1}}$, which is identical to the experiments. The initial chemical composition employed for the numerical simulations and kinetic parameters of the reaction is tabulated in Table 4.

Table 4: Chemical composition and reaction parameters for modelling species transport distribution in the reactor

Parameter	Value	Unit	Reference
$Ca^{2+}_{(aq)}$	0.042	mol L^{-1}	From experiments.
$CO^{2-}_{3(aq)}$	0.042	mol L^{-1}	From experiments.
$CaCO_{3(aq)}$	0	-	—
Activation energy	5.25×10^{6}	J $(kgmol)^{-1}$	[9]
Pre-exponential factor	1.10×10^{8}	s^{-1}	[10]
Mass diffusivity	8.10×10^{-10}	$m^2\ s^{-1}$	[11]

Initially, the reactor is filled with $Ca^{2+}_{(aq)}$; solid calcium carbonate forms as the $CO^{2-}_{3(aq)}$ is diffused at the inlet location by the hydrodynamics condition in the reactor (reagent is introduced in batch mode). A momentum source subroutine is applied at the feed location, which periodically perturbates the velocity magnitude of the feed region by 10 – 15 % of the mean velocity.

Fig. 24 shows the distribution of $CaCO_3$ at different times during the simulation at 100 RPM mixing speed. Given that the mean flow velocity has a clock-wise direction with a central vortex, and reagent addition is right below the surface, the distribution of the reaction plane (i.e., formation of $CaCO_3$) takes a relatively long time to reach the bottom sections. The approach is beneficial for tomographic installation around the reactor.

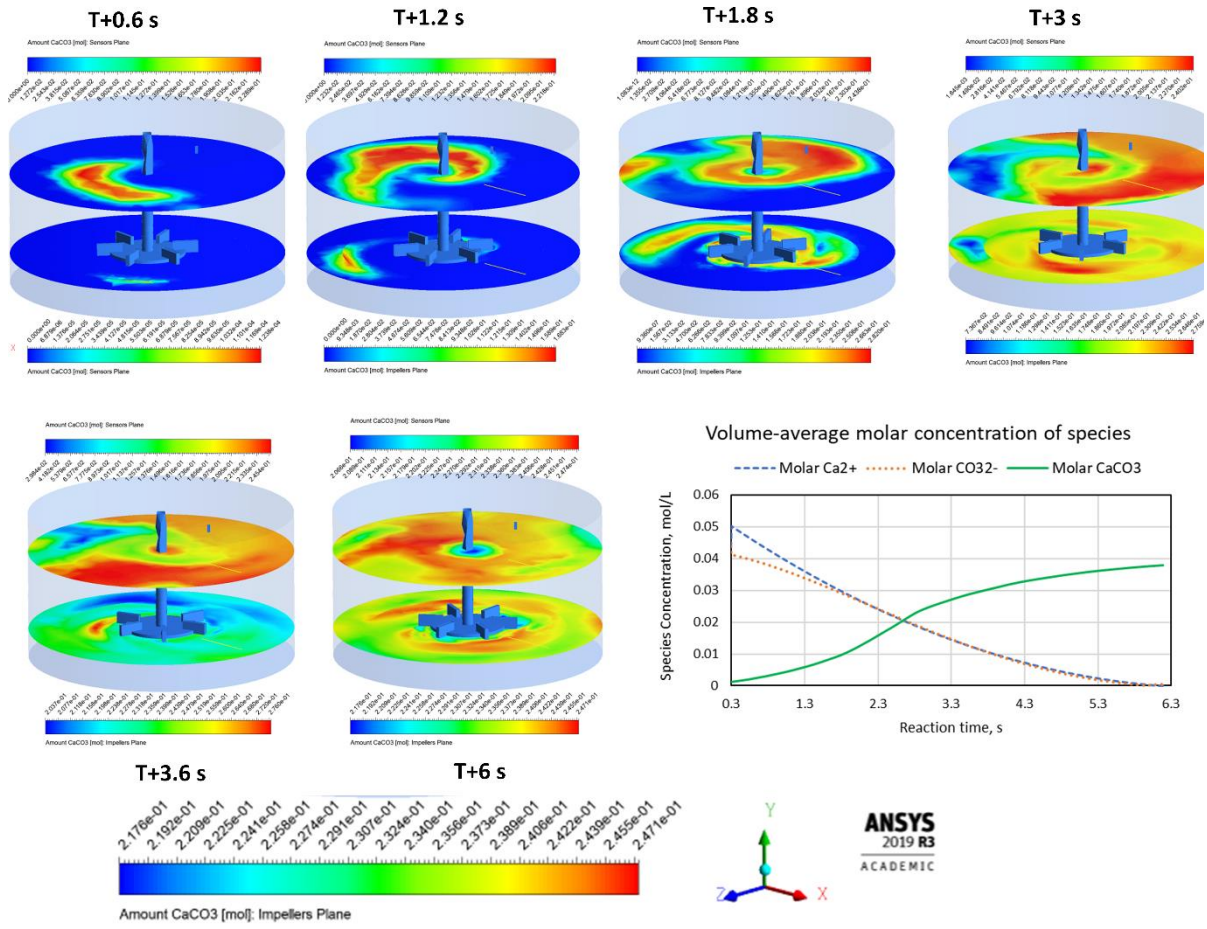

Fig. 24: Volume-average molar concentration of species and spatio-temporal distribution of calcium carbonate in the stirred tank reactor. The mixing speed is 100 RPM with sliding mesh.

4.7.4. Size distribution of particles based on the Rosin-Rammler distribution method

The current framework to evaluate the size distribution is established based on the following assumptions:

(i) Crystallization reaction is instantaneous, and the reactor is well-mixed.

(ii) Reactant supply to crystal surface is diffusion-limited, which results in a size-independent crystal growth mechanism [8].

(iii) One-way coupling (Stokes number << 1); the continuous phase flow pattern is not impacted by the particles; hence, no momentum exchange occurs.

(iv) Flow rate of the reagent to the reactor is constant and continuous; effects of volume increase are negligible, and simulations are carried out at a constant volume level.

As presented in Table 5, calcium carbonate crystallization experiments are carried out at three different mixing speeds; the corresponding volume-averaged dissipation energy is used to obtain the R-R correlations for parameters of n and $\bar{d}$.

Table 5: Experimental data of the crystallization process and the correlations for Rosin-Rammler parameters

Mixing speed, rpm	**Volume-averaged Dissipation energy from torque measurement $[m^2\ s^{-3}]$**	**Averaged spread parameter, n**	**Averaged mean diameter factor, $\bar{d}$ [m]**
100	0.0130	4.22	6.66×10^{-6}
200	0.1037	3.20	7.90×10^{-6}
300	0.3500	3.12	8.9×10^{-6}

Experimental Rosin-Rammler correlation for n	Experimental Rosin-Rammler correlation for $\bar{d}$
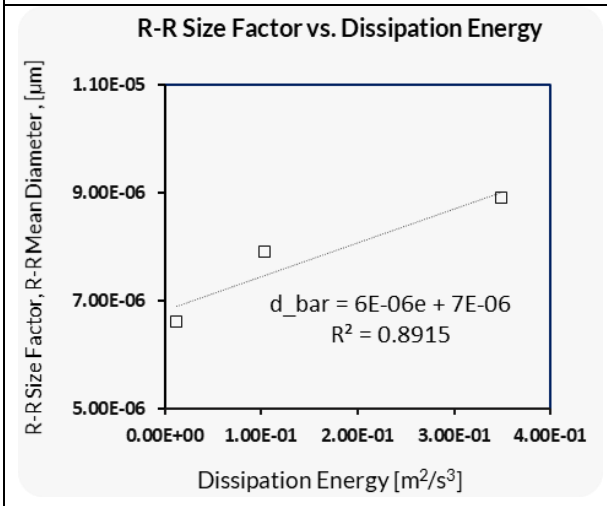	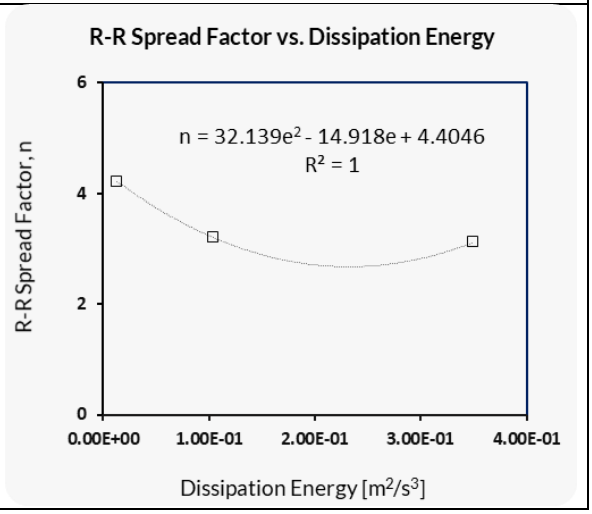

The size distribution equations within the user-defined subroutines take the averaged turbulence dissipation energy of the computational cells as the input and estimate the mass fraction in each cell. Fig. 25 displays the mass fraction of solids at a sampling time of 4.2 s after the start of the chemical reaction at the position of z/H=0.73 and z/H=0.19 (H=105.8 mm, domain height). The calculated mass fraction, which is highly dependent on the mean dissipation energy (ϵ) of the flow field, is in good agreement with the experimental dataset.

The spatial discretization used in the CFD simulations could underpredict the local dissipation energy; however, since the experimental correlations are valid for a relatively wide range of ϵ, the mass fraction estimation is not greatly affected. The accuracy of the ϵ estimation is under further development; for instance, deriving a dimensionless scale factor to increase the accuracy of the cell-based ϵ averaging.

Fig. 26 shows the overall flow field around the mixing plane, which is presented in terms of the velocity magnitude contours. The velocity field is obtained by the SAS turbulence model at 100 RPM. The SAS model can resolve the details of the turbulence structures and predict dissipative trailing edge vortices, which is a prominent feature of the flow field (Fig. 26b). The higher

This project has received funding from the European Union's Horizon 2020 research and innovation programme under the Marie Skłodowska-Curie Grant Agreement No. 764902.

accuracy of the SAS model arises due to its capability in capturing the essential flow features and resolving the spectral dynamics of the flow field.

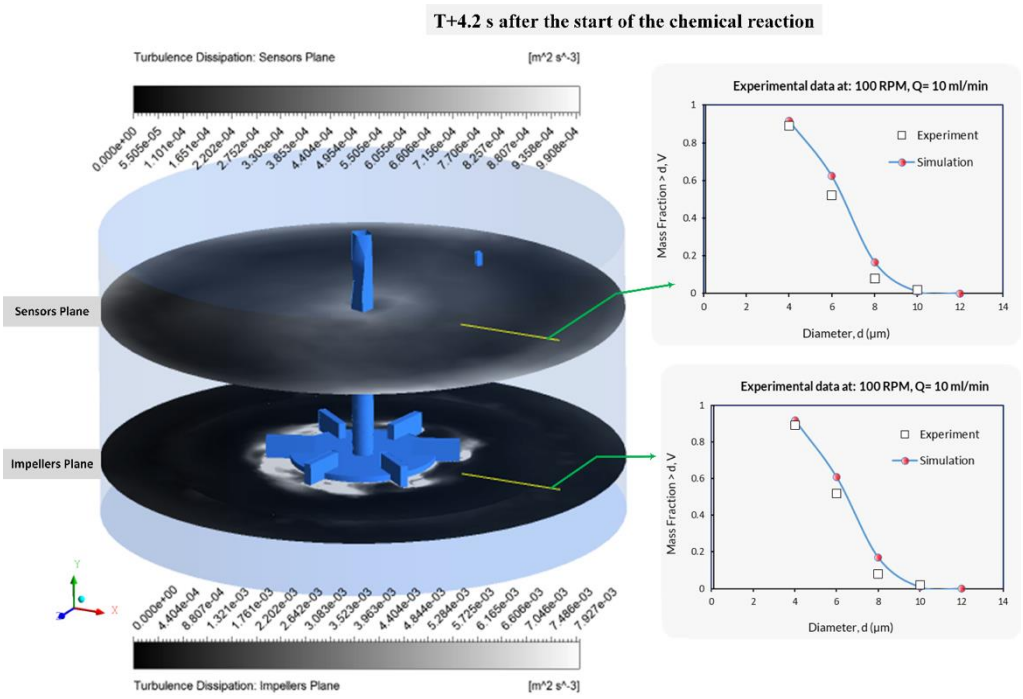

Fig. 25: Counters of the mean dissipation energy (ϵ) of the flow field at two mixing planes at time 6.4 s after the start of the chemical reaction. The mixing speed is 100 RPM. Mass fraction of solid particles is sampled at two radial locations.

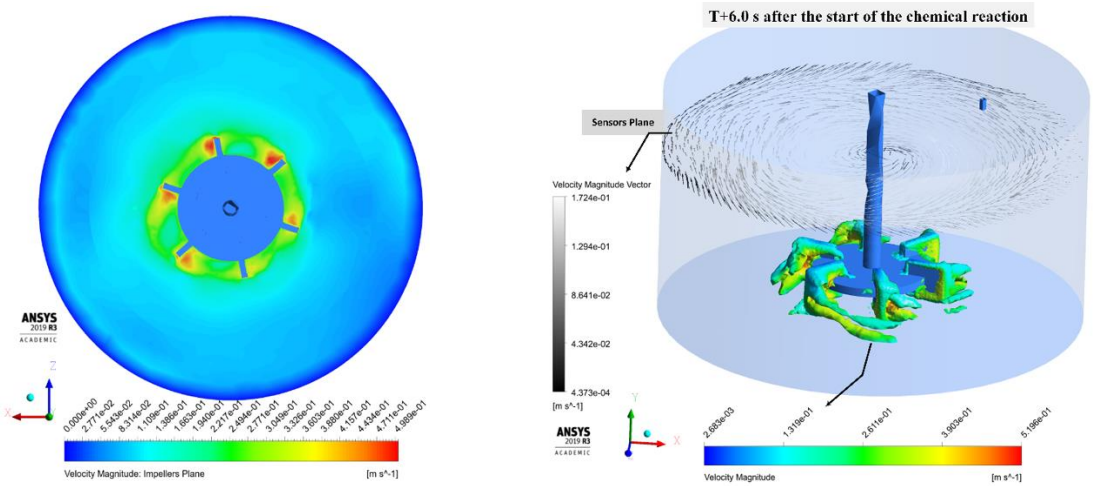

(A) (B)

This project has received funding from the European Union's Horizon 2020 research and innovation programme under the Marie Skłodowska-Curie Grant Agreement No. 764902.

Fig. 26: Six seconds after the start of the chemical reaction at a mixing speed of 100 RPM with the SAS model. (A): Top-view of the contours of velocity magnitude (U_{mag}). (B): 3D trajectories of vorticity structure at the trailing edge of the impeller blades, colored by velocity magnitude.

4.8. Conclusion

Numerical simulations of a crystallization process at 100 RPM are presented in this report. The main objective of the current approach is to simplify the integration and use of experimental information in CFD simulations. Experimental data is fitted to the Rosin-Rammler-based functions and implemented in the CFD software as transport equations. Correlated equations are highly dependent on the discrete size class and turbulence dissipation energy, ϵ. Improving the accuracy of the latter one (i.e., ϵ) is under further investigation. Numerical simulations can be further expanded by using Euler-Lagrange particle tracking to model the particles inside the domain. However, further research is required to develop the model. Additionally, qualitative ultrasound and electrical tomography reconstructions are proposed as a means to validate the CFD simulation based on the species distribution in the flow field.

4.9. References

1. P. Koulountzios, T. Rymarczyk, M. Soleimani, Ultrasonic Time-of-Flight Computed Tomography for Investigation of Batch Crystallisation Processes, Sensors, 21, 639, doi:10.3390/s21020639 (2021).

2. A. Delafosse, A. Line, J. Morchain, P. Guiraud, LES and URANS Simulations of Hydrodynamics in Mixing Tank: Comparison to PIV Experiments, Chemical Engineering Research and Design, 86, 1322–1330, doi:10.1016/j.cherd.2008.07.008 (2008).

3. D. Wilcox, Turbulence Modeling for CFD, 2nd ed., DCW Industries: La Canada Calif., ISBN 9781928729105 (1998).

4. F.R. Menter, Two-Equation Eddy-Viscosity Turbulence Models for Engineering Applications, AIAA Journal, 32, doi:10.2514/3.12149 (1994).

5. F.R. Menter, Y. Egorov, The Scale-Adaptive Simulation Method for Unsteady Turbulent Flow Predictions. Part 1: Theory and Model Description, Flow, Turbulence and Combustion, 85:1, 113–138, doi:10.1007/S10494-010-9264-5 (2010).

6. M. Alderliesten, Mean Particle Diameters. Part VII. The Rosin-Rammler Size Distribution: Physical and Mathematical Properties and Relationships to Moment-Ratio Defined Mean Particle Diameters, Particle & Particle Systems Characterization, 30, doi:10.1002/ppsc.201200021 (2013).

7. H. Wang, Z. (John) Zhai, Analyzing Grid Independency and Numerical Viscosity of Computational Fluid Dynamics for Indoor Environment Applications, Building and Environment, 52, doi:10.1016/j.buildenv.2011.12.019 (2012).

8. D.E. Kile, D.D. Eberl, On the Origin of Size-Dependent and Size-Independent Crystal Growth: Influence of Advection and Diffusion, American Mineralogist, 88, doi:10.2138/am-2003-1014 (2003).

This project has received funding from the European Union's Horizon 2020 research and innovation programme under the Marie Skłodowska-Curie Grant Agreement No. 764902.

9. Q. Li, Y.-S. Jun, The Apparent Activation Energy and Pre-Exponential Kinetic Factor for Heterogeneous Calcium Carbonate Nucleation on Quartz, Communications Chemistry, 1, doi:10.1038/s42004-018-0056-5 (2018).

10. M. Ramezani, P. Tremain, E. Doroodchi, B. Moghtaderi, Determination of Carbonation/Calcination Reaction Kinetics of a Limestone Sorbent in Low CO2 Partial Pressures Using TGA Experiments. Energy Procedia, 114, doi:10.1016/j.egypro.2017.03.1168 (2017).

11. R.E. Zeebe, On the Molecular Diffusion Coefficients of Dissolved, and Their Dependence on Isotopic Mass, Geochimica et Cosmochimica Acta, 75, doi:10.1016/j.gca.2011.02.010 (2011).

This project has received funding from the European Union's Horizon 2020 research and innovation programme under the Marie Skłodowska-Curie Grant Agreement No. 764902.